Role of the crystal electric field on the two magnetic transitions in the orthorhombic $YbMnO_3$ perovskite

Jingsan Hu,[1] Guannan Li,[1,2] Xiaokun Huang,[1] and Weiyi Zhang[1,3,*]

[1]*National Laboratory of Solid State Microstructures and Department of Physics, Nanjing University, Nanjing 210093, China*

[2]*Department of Physics, Huaiyin Institute of Technology, Huaian 223003, China*

[3]*Collaborative Innovation Center of Advanced Microstructures, Nanjing 210093, China*

(Received 30 November 2018; revised manuscript received 22 February 2019; published 11 April 2019)

In orthorhombic $LuMnO_3$ perovskite with nonmagnetic Lu^{+3} ions ($4f^{14}5d^06s^0$) there exists one magnetic transition of Mn^{+3} ions at $T_N \approx 35.5$ K. In $YbMnO_3$ perovskite with Yb^{+3} ions of one electron less ($4f^{13}5d^06s^0$), two magnetic transitions are observed at $T_N \approx 43$ K and $T \approx 3$–4 K, respectively. While the transition at 43 K in $YbMnO_3$ was attributed to the same magnetic ordering of Mn^{+3} moments as $LuMnO_3$ at 35.5 K, the nature of the magnetic transition at 3–4 K is still unresolved. Although the bump feature in magnetic susceptibility hints at a possible antiferromagnetic ordering of Yb^{+3} ions, no clear magnetic ordering of Yb^{+3} was determined in either neutron scattering diffraction or in Mössbauer spectra of iron-doped $YbMnO_3$. To explain the amplitude-modulated nature of the low magnetic anomaly, we propose in this paper that a gradual quenching of the orbital moment of Yb^{+3} ions below a critical temperature is a possible mechanism. The small crystal field splitting of $4f$ electrons can survive only at extremely low temperature because of thermal fluctuation. In addition, we show, like in $LuMnO_3$, that $YbMnO_3$ takes an E-type antiferromagnetic ground state for its Mn ions and can be tuned into ferromagnetic state when (110)-oriented $YAlO_3$ is used as a substrate.

DOI: 10.1103/PhysRevB.99.134418

I. INTRODUCTION

Perovskite compounds with chemical formula ABO_3 are a large class of materials in nature with rich functionalities [1,2]. Ferroelectric $BaTiO_3$, $PbTiO_3$ compounds [1], and colossal magnetoresistance compounds $La_{1-x}Ba_xMnO_3$ [2] are just a few typical examples which are widely applied in transducers, actuators, capacitors, memories, and small magnetic sensors. Because of the novel quantum phenomena revealed by manganite based perovskite compounds due to the strong competition among its charge, spin, and orbital degrees of freedom, extensive experimental and theoretical studies have been carried out on the structural, electronic, and magnetic properties of almost complete rare-earth series.

The manganite based perovskite compounds can exist in nature either in orthorhombic phase (o-$RMnO_3$) with $Pbnm$ space group or in hexagonal phase (h-$RMnO_3$) with $P63cm$ space group depending on the ionic radius of rare-earth elements [3,4]. $RMnO_3$ family takes an o-$RMnO_3$ structure for rare-earth atoms R = La-Dy with large radius [5,6]. They are nonferroelectric magnetic compounds because structures preserve centrosymmetric property. The magnetic structures mainly take a planar antiparallel magnetic structure (A-AFM) with weak ferromagnetism arising from a small canted magnetic moment along the crystal b axis. On the other hand, the h-$RMnO_3$ structure is preferred for rare-earth atoms R = Ho-Lu, Y, and Sc with small radius. Strong deviation from an ideal tolerance factor breaks centrosymmetry and a 120° arranged complex magnetic structure of Mn ions further enhances the multiferroic properties with simultaneous ferroelectric and magnetic orderings [7]. However, the hexagonal perovskites with small rare-earth atoms can be converted into metastable orthorhombic perovskites if high pressure and high temperature are applied during sample preparation [4]. It is also possible to fabricate orthorhombic perovskites of R = Y, Ho, and Er using the low temperature soft-chemistry route or the epitaxial deposition method on substrates. When hexagonal perovskite is transformed into orthorhombic perovskite, the noncollinear 120° oriented magnetic structure is also changed into an E-type antiferromagnetic structure (E-AFM).

For the manganite based perovskites with rare-earth atoms, magnetic properties are contributed by both transition-metal Mn and rare-earth R except those with closed $4f$ orbitals. For a single transition-metal (rare-earth) ion, the magnetic moment of an ion is simply determined by Hund's three rules, i.e., spin and orbital angular momenta are maximized, and spin and angular momenta are aligned antiparallel (parallel) if the $3d$ ($4f$) shell is below (above) half-filled. However, when magnetic ions form a building block of crystal compounds, the crystal electric field of other atoms lowers the local symmetry around the magnetic ions and spherical harmonics cease to be the eigenfunctions of atoms [8,9]. Quantum mechanically speaking, the orbital angular momentum is either completely or partly quenched depending on the crystal symmetry. This is particularly true for transition-metal Mn-d ions. $3d$-orbital wave functions spread relatively broadly with respect to the lattice constant. The crystal field splitting (CFS) is of the order of eV and much larger than room temperature thermal fluctuation and spin-orbit coupling strength. Thus, CFS is almost independent of temperature and the orbital angular moment remains quenched throughout room temperature. The

*wyzhang@nju.edu.cn

situation is more subtle for R ions because their wave functions are very localized around ions and spin-orbit coupling strength is large. CFS in this case is two orders of magnitude smaller than that of transition-metal ions and is vulnerable to thermal fluctuation. It is, therefore, possible at some temperature that thermal fluctuation overcomes CFS and restores orbital magnetic moments with the help of strong spin-orbit coupling. This is, in fact, true to many rare-earth ions showing the paramagnetic moments dictated by the Hund's rule.

The motivation of the present study stems from the systematic investigations of magnetic properties of $YbMnO_3$ over the past five decades and particularly revelent low temperature results are only available recently. The early magnetic measurement was carried out by Wood *et al.* in 1973 in which magnetic susceptibilities showed antiferromagnetic features for both hexagonal and orthorhombic perovskites [3]. The derived Curie temperature and paramagnetic moment are $\theta = -200$ and -83 K and $\mu_{\text{eff}} = 6.63$ and 6.72 μ_B for hexagonal and orthorhombic phases, respectively. The paramagnetic moments are very close to the geometrical sum of the theoretical values of Mn^{+3} and Yb^{+3} ions, $\mu_{\text{eff}} = \sqrt{(\mu_{\text{eff}}^{\text{Mn}})^2 + (\mu_{\text{eff}}^{\text{Yb}})^2} = 6.68\ \mu_B$. $\mu_{\text{eff}}^{\text{Mn}} = 4.9\ \mu_B$ is the paramagnetic moment of Mn^{+3} ions of spin only while $\mu_{\text{eff}}^{\text{Yb}} = 4.54\ \mu_B$ is the paramagnetic moment of Yb^{+3} ions including both spin and orbital magnetic moments. No ordering was observed directly in either phases above 4.2 K. In a recent experimental investigation, two magnetic transitions were observed by Huang *et al.* for both structural phases of $YbMnO_3$ [4]. The transition temperatures are 43 and $\approx$4 K for *o*-$YbMnO_3$ and 88 and $\approx$4 K for *h*-$YbMnO_3$. The high magnetic transitions are characterized by small kicks in the derivative of susceptibility and were attributed to the paramagnetic to an E-type antiferromagnetic structure (E-AFM) of Mn^{+3} ions in *o*-$YbMnO_3$ and paramagnetic to a 120° aligned magnetic structure of Mn^{+3} ions in *h*-$YbMnO_3$. The low magnetic anomalies in susceptibility at 4 K were assigned to an unspecified AFM ordering of Yb^{+3} moments though no Yb^{+3} sublattice ordering was directly observed. The assignment was made because the paramagnetic moment μ_{eff} below the high transition temperature 4.83 and 3.8 μ_B is close to 4.54 μ_B, the paramagnetic moment of Yb^{+3} ions.

To shed light on the underlying mechanism behind the low magnetic anomaly of manganite based perovskites with rare-earth atoms, electromagnon spectra, a unique type of polar coupled magnons in multiferroics, offer valuable insights on the magnetic couplings among Mn and Yb ions as well as the crystal electric field effect on magnetic ions. Previous polarized inelastic neutron scattering studies revealed that electromagnon has a hybrid character of magnetic spin wave and a lattice vibration [10,11]. By adopting a single crystal sample of *h*-$YbMnO_3$, Standard *et al.* [12] were able to map the electromagnon frequencies as functions of temperature and external magnetic field. At low temperatures, a single magnon in $YbMnO_3$ splits into several distinct adsorption lines at $T_{\text{Yb}} = 3.3$ K. The extracted internal magnetic fields associated with magnon splitting showed monotonically decreasing functions with temperature and approach zero at T_{Yb} [see Fig. 7(c) of Ref. [12]). Since Mn^{+3} ions already form an 120° aligned magnetic structure at low temperature, the magnon mode splitting can only arise from magnetic configuration change of Yb^{+3} ions. As Yb^{+3} ions are paramagnetic in the temperature range 6–30 K above T_{Yb} [4], they assigned low temperature spin configuration of Yb^{+3} ions as an antiferromagnetic structure. The same scenario was assumed for the low magnetic transition in *o*-$YbMnO_3$. In fact, the magnon splitting below T_{Yb} only states that the magnetic couplings between Mn^{+3} spins and Yb^{+3} spins are isotropic above T_{Yb} while anisotropic couplings are present below T_{Yb}. The anisotropic coupling can be brought about by magnetic ordering of Yb spins below T_{Yb} or possibly by other mechanisms as well.

Although the above discussions concentrated on manganite based perovskites with rare-earth Yb [13,14], the low magnetic anomaly is, in fact, a common phenomenon for manganite based perovskites with all rare-earth ions with a partially filled $4f$ shell [15–17]. $LuMnO_3$ compound is an exception because Lu^{+3} has a closed $4f$ shell [18,19]. For example, a low magnetic anomaly was also observed at 5 K in *h*-$HoMnO_3$ [15], at 7 K in *o*-$TbMnO_3$ [16], and at 15 K in $ErMnO_3$ [17]. The low magnetic anomalies are also accompanied by thermodynamical anomalies. The magnetic-related specific heat showed sharp narrow peaks at the same transition temperatures [15–17]. In addition to the manganite based perovskites with rare-earth atoms, a low magnetic anomaly has also been observed in rare-earth dodecaborides RB_{12} (R = Y, Tb-Tm) [20]. Like Yb in manganite based perovskites, Tb-Tm ions in dodecaborides also have a valence state R^{+3}. Two of the donated electrons go to the valence bands formed by a body-centered-cubic lattice of B_{12} cubes while another electron goes to the conduction band with strongly hybridized characters of R-5d and B-2p. However, R-4f orbitals lay well below the Fermi energy, thus the R-4f shell is well localized and virtually decoupled from the rest of the electronic bands. The inelastic neutron scattering measurement revealed an amplitude modulated magnetic transition at a critical temperature monotonically decreasing with decreasing R radius. The phase transition is also confirmed by a sharp peak in specific heat measurement. Since it was not clear how an amplitude modulated magnetic moment of R is brought about, a paramagnetic to antiferromagnetic transition was also assumed as a cause.

From the above discussions, it is clear that the low magnetic anomaly in manganite based perovskites and magnetic transition in dodecaborides are closely correlated to the spin configuration change of R^{+3} ions. However, less is known whether the transition is brought about by spontaneous antiferromagnetic ordering or caused by spontaneous quenching of orbital magnetic moments of rare-earth ions or by their combined effects. Up to now, there is no consensus on sublattice ordering of R ions [21,22]. Mössbauer spectral measurement on Fe doped *o*-$YbMnO_3$ concluded that Yb^{+3} electronic states are well localized and no Yb sublattice ordering is observed above 1.8 K [23]. From a structural point of view, antiferromagnetic orderings of R moments in E-AFM *o*-$RMnO_3$ perovskites involves a highly frustrated environment of a Mn sublattice. It is not clear what kind of complex antiferromagnetic structure of R ions can conform with the surrounding Mn spin configuration. The situation holds also for RB_{12} dodecaborides where a conducting network formed

by fcc B_{12} cubes effectively blocks the coupling between neighboring R ions. Summarizing the above discussions, the low magnetic anomaly involves strong spin-lattice coupling as manifested by the electromagnon spectra, the amplitude modulated magnetic moments of R ions further indicated that the crystal electric field effect on orbital magnetic moment quenching is a possibility. In addition, the susceptibilities of some of manganite based perovskites showed an upturn below the low magnetic anomalies which are contradictory to the antiferromagnetic transition [12,13,15,16]. So it is natural to ask whether the low magnetic anomaly can result from the magnetic moment change of individual rare-earth ions.

Since the low magnetic anomaly occurs at very low temperature for very localized $4f$-shell rare-earth ions, CFS is very small and susceptible to thermal fluctuation. We propose that the excitation of thermal phonons tends to isotropize the crystal electric field (CEF) and destroys CFS at a critical temperature. This makes the CFS from a quantum mechanic quantity to a thermodynamic order parameter. In our model, the rare-earth ions behave like paramagnetic ions above the transition with the total magnetic moment dictated by the Hund's three rule while the orbital magnetic moment are completely or partially quenched below the transition depending on the local crystal symmetry around ions. With this picture, the CFS order parameter can easily account for the strong spin-lattice coupling, the amplitude modulated nature, as well as the specific heat and susceptibility jumps associated with the low magnetic anomalies. Our rough estimate yields a critical temperature consistent with the experimental observations. We would like to emphasize that our model focused on the common low magnetic anomaly itself. We do not intend to explore the specific magnetic structure below the low temperature magnetic anomaly. Currently, both upturn and downturn susceptibilities are observed below the low magnetic anomaly [4,12–15], the exact magnetic structure below the low magnetic anomaly depends on the subtle competition among magnetic couplings between rare-earth ions and between rare-earth and manganite ions which is case specific.

As the crystal field splitting energy is proportional to $\langle r^4\rangle/d^5$ with $\langle r^4\rangle$ and d denoting the fourth moment of $4f$ orbitals and bond length with nearest neighbors, rare-earth ions with larger $\langle r^4\rangle$ and smaller d are predicted to have higher transition temperature if the same crystal structures are preserved. This is in fact proved to be true in manganite based perovskites with rare-earth ions (R = Y, Ho-Lu). In addition, the external strain imposed by either hydrostatic pressure [24] or substrates [25–27] also have a significant effect on the magnetic transition of manganite based perovskite. The hydrostatic pressure is predicted to induce a ferromagnetic to antiferromagnetic transition in a Sr-doped $La_{0.625}Sr_{0.375}MnO_3$ compound [24]. The tetragonal strain, in turn, tunes ferromagnetic and antiferromagnetic exchange couplings by controlling the orbital ordering of Mn-$d(e_g)$ orbitals [25–27]. Just like the E-AFM antiferromagnetic structure can be tuned into a ferromagnetic structure if (110) oriented $YAlO_3$ substrate is applied to $LuMnO_3$. We found that the same substrate is also capable of realizing the ferromagnetic structure in $YbMnO_3$.

Although the concept we proposed in this paper applies to all transition-metal based perovskites with rare-earth ions, we shall concentrate below only on the orthorhombic $YbMnO_3$ compound. First, the magnetic structure in o-$YbMnO_3$ is simpler and involves mainly collinear magnetic structure in low temperature while h-$YbMnO_3$ involves a 120° noncollinear spin rotated magnetic structure. Second, the local crystal symmetry of R ions in o-$YbMnO_3$ is high which simplifies the crystal electric potential computation and estimation of critical temperature caused by thermal fluctuation. Third, Yb^{+3} ions have a very simple electronic structure with one electron missing in the closed $4f$ shell, the $4f$ shell can be described by a single hole representation which considerably simplifies the calculations of magnetic and thermodynamical quantities. This enables one to see how the crystal field splitting energy, spin-orbit coupling energy, and Zeeman splitting energy collectively make the low magnetic anomaly happen in paramagnetic rare-earth ions.

The rest of the paper is organized in following way. As the magnetic properties of $YbMnO_3$ are divided into the two parts associated with Yb ion and Mn ions, in Sec. II we first present the Hamiltonian of the paramagnetic Yb ions in o-$YbMnO_3$ including a local crystal field splitting term, spin-orbit coupling term, as well as the Zeeman splitting term under magnetic field. Each term is discussed regarding their magnitudes and their sensitivities to thermal fluctuation effect. In particular, why the CFS of Yb^{+3} ions should be treated as a thermodynamical quantity of temperature rather than as a quantum mechanical quantity is emphasized. Special attention is paid on the thermal fluctuation on CFS and critical temperature estimation. The Mn-ions related magnetic structures are analyzed within the framework of density-functional theory, the crystal structure, types of magnetic structures, as well as the relevant parameters setting are discussed in Sec. III. The susceptibility and specific heat of rare-earth ions and Mn-ion magnetic ground state are presented in Sec. IV. We illustrated how the low magnetic anomaly arises naturally when the CFS is treated as an order parameter. We also showed how the E-AFM structure is converted into a FM structure when $YbMnO_3$ is under an in-plane epitaxial strain pattern imposed by a (110)-oriented $YAlO_3$ substrate. Section V is our conclusion.

II. MODEL HAMILTONIAN OF PARAMAGNETIC Yb IONS

The Hamiltonian of paramagnetic rare-earth ions is well known and involves three competing interaction terms,

$$H_0 = H_{SO} + H_{CF} + H_{ZS}, \tag{1}$$

i.e., spin-orbit coupling (H_{SO}), crystal field splitting (H_{CF}), as well as the Zeeman splitting energy under external magnetic field (H_{ZS}). $H_{SO} = \xi \mathbf{L}\cdot\mathbf{S} = 0.5\xi[J(J+1) - L(L+1) - S(S+1)]$ describes the energy for parallel or antiparallel alignment of ionic spin and orbital angular momentums. ξ is the spin-orbit coupling constant. This term is the largest in energy ($\xi = -0.37$ eV) [28,29] and its matrix is diagonal in total angular momentum space $|JM_J\rangle$. For the specific case of Yb^{+3} ions, $L = 3$, $S = 1/2$. The diagonal matrix elements are either 1.5ξ for $J = 7/2$ multiplicity (eightfold states) or -2ξ for $5/2$ multiplicity (sixfold states) with corresponding Landé factor $g = 8/7$ and $7/6$, respectively. However, to conform with the Hamiltonian of the crystal field splitting term, it

is better to write the spin-orbit Hamiltonian in a product space $|Y_{\mathrm{LM}}\sigma\rangle$ of spin ($\sigma = \pm 1$) and orbital (Y_{LM}). The matrix element takes a following form:

$$\begin{aligned}&\langle Y_{\mathrm{LM}'}\sigma'|H_{\mathrm{SO}}|Y_{\mathrm{LM}}\sigma\rangle \\ &\quad = 0.5\xi[\sqrt{(L-\sigma M)(L+\sigma M+1)}\delta_{M'M+\sigma}\delta_{\sigma'\bar{\sigma}} \\ &\qquad + \sigma M\delta_{M'M}\delta_{\sigma'\sigma}]. \end{aligned} \tag{2}$$

For a magnetic field $\mathbf{B}$ with an orientation $\hat{\tau} = (\alpha, \beta, \gamma)$, Zeeman splitting term $H_{\mathrm{ZS}} = -\mu_B\mathbf{B}\cdot[\mathbf{L}+2\mathbf{S}]$ can also be expressed easily in the spin-orbital product space

$$\begin{aligned}&\langle Y_{\mathrm{LM}'}\sigma'|H_{\mathrm{ZS}}|Y_{\mathrm{LM}}\sigma\rangle \\ &\quad = -\mu_B B[0.5(\alpha - i\beta)\sqrt{(L-M)(L+M+1)}\delta_{M'M+1}\delta_{\sigma'\sigma} \\ &\qquad + 0.5(\alpha + i\beta)\sqrt{(L+M)(L-M+1)}\delta_{M'M-1}\delta_{\sigma'\sigma} \\ &\qquad + (\alpha + i\sigma\beta)\delta_{M'M}\delta_{\sigma'\bar{\sigma}} + \gamma(M+\sigma)\delta_{M'M}\delta_{\sigma'\sigma}]. \end{aligned} \tag{3}$$

The crystal field splitting Hamiltonian is usually written in terms of crystal wave functions. Assuming a cubic symmetry for the Yb^{+3} ions of orthorhombic perovskite with 12 nearest-neighbors oxygen ions, crystal wave functions can be expanded in terms of spherical harmonics $f_{xyz} = (Y_{32} - Y_{3\bar{2}})/\sqrt{2}\,(i=1)$, $f_{x(y^2-z^2)} = (\sqrt{3}Y_{33} + \sqrt{5}Y_{31} - \sqrt{5}Y_{3\bar{1}} - \sqrt{3}Y_{3\bar{3}})/2 \quad (i=2)$, $f_{y(z^2-x^2)} = (\sqrt{3}Y_{33} - \sqrt{5}Y_{31} - \sqrt{5}Y_{3\bar{1}} + \sqrt{3}Y_{3\bar{3}})/2 \ (i=3)$, $f_{z(x^2-y^2)} = (Y_{32} + Y_{3\bar{2}})/\sqrt{2} \ (i=4)$, $f_{x(5x^2-3r^2)} = (\sqrt{5}Y_{33} - \sqrt{3}Y_{31} + \sqrt{3}Y_{3\bar{1}} - \sqrt{5}Y_{3\bar{3}})/2 \ (i=5)$, $f_{y(5y^2-3r^2)} = (\sqrt{5}Y_{33} + \sqrt{3}Y_{31} + \sqrt{3}Y_{3\bar{1}} + \sqrt{5}Y_{3\bar{3}})/2 \ (i=6)$, $f_{z(5z^2-3r^2)} = Y_{30} \ (i=7)$. The Hamiltonian is diagonal

$$H_{\mathrm{CF}} = \sum_{i=1}^{7} J_i f_{i\sigma}^{\dagger} f_{i\sigma}, \tag{4}$$

with on-site energy corrected by CFS J_i. Here $f_{i\sigma}$ denotes the annihilation operator of a single electron in state i of the Yb^{+3} ions. For cubic symmetry, f orbitals are split into one singlet and two triplets. If we take the on-site energy of the singlet as an energy reference ($J_1 = 0$), $J_2 = J_3 = J_4 = \Delta_1$, and $J_5 = J_6 = J_7 = \Delta_2$ with Δ_1 and Δ_2 specifying a crystal splitting pattern. In the case that only the fourth order term of the crystal electric potential is considered, $\Delta_1 = 5Dq$ and $\Delta_2 = 9Dq$ with $9Dq$ denoting the total span of $4f$ orbitals. When both fourth and sixth order terms are considered, the crystal splitting pattern of YB-$4f$ orbitals are not altered, but no longer described by a single parameter Dq. In general, the CFS parameters have to be evaluated from the crystal electric potential (CEP) of Yb^{+3} ions:

$$\begin{aligned}V(\mathbf{r}) = &\frac{\alpha e^2}{4\pi\epsilon_0 a_0} - \frac{35Ze^2}{4\pi\epsilon_0\sqrt{2}a_0^5}\left[(x^4+y^4+z^4) - \frac{3}{5}r^4\right] \\ &+ \frac{273\sqrt{2}Ze^2}{4\pi\epsilon_0 a_0^7}\left[(x^6+y^6+z^6) + \frac{15}{4}\left(x^2y^4 + x^2z^4\right.\right. \\ &\left.\left. + y^2x^4 + y^2z^4 + z^2x^4 + z^2y^4\right) - \frac{15}{14}r^6\right]. \end{aligned} \tag{5}$$

Here the first term is the long range Coulomb contribution to a f electron of Yb^{+3} ions by all the ions in a crystal. The second (fourth-order) and third (sixth-order) terms are the short range terms contributed only by nearest neighbor oxygen ions. Z is the valence of oxygen ions and a_0 is the lattice constant of the pseudocubic cell of $YbMnO_3$. Assuming an ionic picture of Yb^{+3}, O^{-2}, and Mn^{+3}, $\alpha = 1.85547$ is obtained for summing over a whole crystal while $\alpha = -12\sqrt{2}Z = 24\sqrt{2} = 33.9413$ if only the nearest oxygen ions ($Z = -2$) are taken into account. As we shall see later, these two values offer useful guidance when estimating the thermal fluctuation effect on small CFS quantity.

By integrating over CEP using the crystal wave functions above, one obtains the crystal splitting parameters

$$\Delta_1^0 = \frac{2Ze^2}{4\pi\epsilon_0\sqrt{2}a_0}\left[\frac{70}{33}\frac{\langle r^4\rangle}{a_0^4} - \frac{210}{11}\frac{\langle r^6\rangle}{a_0^6}\right], \tag{6}$$

$$\Delta_2^0 = \frac{2Ze^2}{4\pi\epsilon_0\sqrt{2}a_0}\left[\frac{42}{11}\frac{\langle r^4\rangle}{a_0^4} - \frac{70}{11}\frac{\langle r^6\rangle}{a_0^6}\right]. \tag{7}$$

Using the lattice parameters $a = 5.2160$ Å, $b = 5.8030$ Å, and $c = 7.2816$ Å obtained at 9 K for the $\sqrt{2}\times\sqrt{2}\times 2$ orthorhombic cell of $YbMnO_3$ [4], $a_0 = \sqrt[3]{abc/4} = 3.806$ Å is extracted. Together with the fourth-moment and sixth-moment parameters, $\langle r^4\rangle = 0.08534$ Å^4 and $\langle r^6\rangle = 0.08634$ Å^6, for YB-f electrons [30], we get rough estimate of the crystal splitting parameters $\Delta_1^0 = -3.436$ meV and $\Delta_2^0 = -14.713$ meV. This suggests that CFS of rare-earth ions is two orders of magnitude smaller than that of transition-metal ions even though purely ionic model usually exaggerate the valence state of ions and CFS parameters. Thus unlike the CFS of transition-metal ions which is of the order of 1 eV and sustainable to high temperature with negligible reduction, the CFS in rare-earth ions is vulnerable to thermal fluctuation. Thermal smearing effect on CFS cannot be ignored and should be considered seriously. In the following, we argue that low temperature thermal lattice vibration competes strongly with the CFS of rare-earth ions. The characteristic temperature above which thermal lattice fluctuation kills CFS defines the transition temperature of low magnetic anomaly.

To see how thermal lattice vibration destroys the CFS of rare-earth ions, it is simple to estimate how a periodically volume expanding and contracting Jahn-Teller mode fluctuates the energy level of $4f$ orbitals. The local potential fluctuation is given by

$$\Delta V(x,y,z) = \frac{\alpha e^2}{4\pi\epsilon_0}\frac{2}{3}\frac{Q_x+Q_y+Q_z}{a_0^2} = \frac{\alpha e^2}{4\pi\epsilon_0}\frac{2}{\sqrt{3}}\frac{Q_1}{a_0^2}. \tag{8}$$

Q_x, Q_y, and Q_z denote the displacements of 12 nearest-neighbor oxygens in their positions while keeping the local symmetry intact. $Q_1 = (Q_x+Q_y+Q_z)/\sqrt{3}$ represents the periodically contracting and expanding mode. Although the effective α responsible for CEP fluctuation is hard to know, it should lie between the nearest-neighbor approximation and exact Madelung constant regarding an electron on Yb ions.

Using the Debye model to describe the low frequency phonon excitation, the standard deviation of Q_1^2 can be obtained as

$$\bar{Q}_1^2 \approx \frac{3\pi^2\hbar^2}{2M_O k_B\theta_D}\left(\frac{T}{\theta_D}\right)^2. \tag{9}$$

Here M_O is the reduced mass of oxygen atoms with respect to its central Yb ions. θ_D is the Debye temperature of the Jahn-Teller mode. Using the Debye temperature $\theta_D \approx$

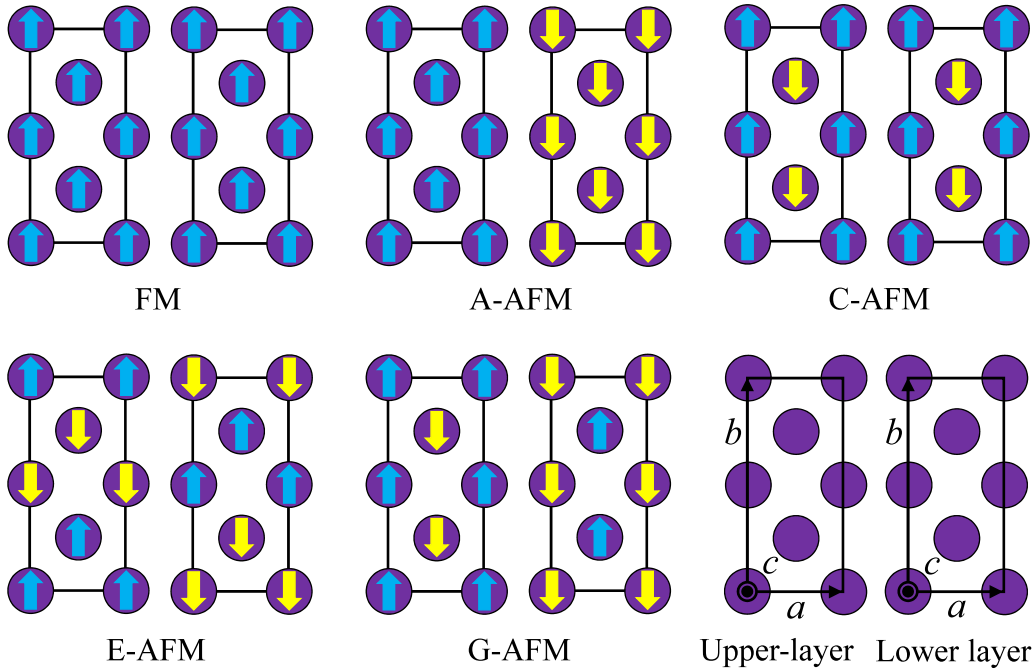

FIG. 1. Schematic diagrams of five typical magnetic structures of Mn ions in $YbMnO_3$: the ferromagnetically ordered structure (FM), the antiferromagnetically ordered nearest-plane (A-AFM), the nearest-chain (C-AFM), the in-plane nearest-zigzag-chain (E-AFM), and the nearest-neighbor (G-AFM) structures. The arrows on Mn ions denote spin directions. The left and right panels refer to the upper and lower layers of the double cell.

345 K [14] and $|\Delta V| \approx |\Delta_2|$, one obtains $T_C \approx 6.6$ K if an exact Madelung constant is used and $T_C \approx 0.36$ K if only the nearest-neighbor oxygen contribution is considered. The transition temperature of the low magnetic anomaly does lie between these two values.

Once the eigenvalues and eigenvectors of the Hamiltonian of a paramagnetic Yb^{+3} ion is specified, it is a simple task to compute the magnetic susceptibility and specific heat as functions of temperature

$$\chi_\tau(T) = \frac{\mu_B}{B} \frac{\sum_n \langle n|\hat{\tau}\cdot(\mathbf{L}+2\mathbf{S})|n\rangle \exp(-E_n/k_BT)}{\sum_n \exp(-E_n/k_BT)} \quad (10)$$

and

$$C_V(T) = \frac{1}{k_BT^2}\left\{\frac{\sum_n E_n^2 \exp(-E_n/k_BT)}{\sum_n \exp(-E_n/k_BT)} - \left(\frac{\sum_n E_n \exp(-E_n/k_BT)}{\sum_n \exp(-E_n/k_BT)}\right)^2\right\}. \quad (11)$$

We will see that gradual quenching of orbital magnetic moments of Yb ions is brought about by the emergence of CFS order parameter below critical temperature. The low magnetic anomaly appears once the CFS parameter is treated as a thermodynamical order parameter with a critical temperature deducted from Eqs. (8) and (9).

III. Mn RELATED MAGNETIC STRUCTURES AND PARAMETER SETTINGS

The metastable orthorhombic perovskite structures of $YbMnO_3$ (o-$YbMnO_3$) can be prepared through a reconstructive transformation from the sol-gel synthesized hexagonal $YbMnO_3$ (h-$YbMnO_3$) by means of high-pressure annealing at 5 GPa and 1100 °C [4]. The crystal structure of o-$YbMnO_3$ was identified by powder neutron diffraction as a space group $Pbnm$ with crystal parameters $a = 5.2160$ Å, $b = 5.8030$ Å, and $c = 7.2816$ Å at 9 K [4]. The unit cell of paramagnetic o-$YbMnO_3$ is composed of $\sqrt{2} \times \sqrt{2} \times 2$ $YbMnO_3$ formula units (20 atoms) as depicted in Fig. 1. The crystal axes **a**, **b**, and **c** are also indicated. In this paper five typical magnetic structures of Mn ions are considered. They include ferromagnetically ordered structure (FM), antiferromagnetically ordered nearest-plane (A-AFM), nearest-chain (C-AFM), nearest-neighbor (G-AFM), and in-plane nearest-zigzag-chain (E-AFM) structures. The crystal unit cell also hosts FM, A-AFM, C-AFM, and G-AFM magnetic structures. The crystal cell of the more complex E-AFM magnetic structure is doubled along the crystal **b** axis and thus contains 40 atoms. When a substrate strain of (110)-oriented $YAlO_3$ is considered on $YbMnO_3$, the crystal symmetry changes from orthorhombic to monoclinic groups. The crystal cell changes from a parallelepipedon formed by **a**, 2**b**, and **c** for bulk to that formed by 2(**a**-**b**), **a**, and **c** for strained samples. In our numerical study, the former unit cell is used to compute the electronic and magnetic properties of bulk o-$YbMnO_3$ compound, while the latter unit cell is used to simulate those of strained monoclinic samples on substrates. The same crystal unit cells are used for all five typical magnetic structures in order to eliminate the systematic error caused by different Wigner-Seitz cells and Brillouin zones.

The relative stabilities of various magnetic structures associated with Mn ions are analyzed using the density-functional theory (DFT) based Vienna *ab initio* simulation package (VASP) [31] with projected augmented wave (PAW)

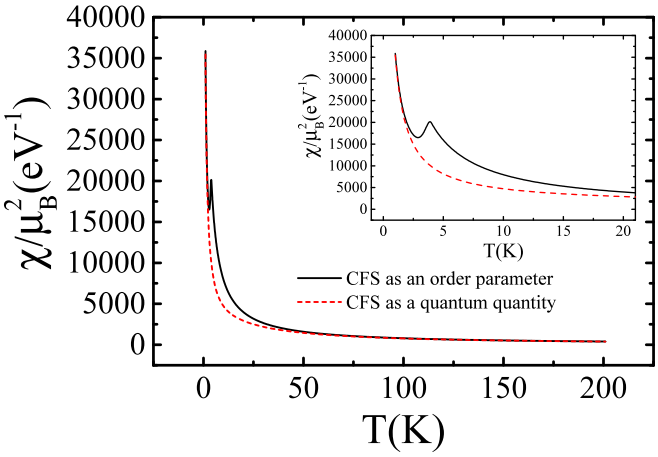

FIG. 2. Magnetic susceptibility per paramagnetic Yb^{+3} ion. The low temperature parts are enlarged in the inset. The dashed line refers to CFS treated as a quantum quantity while the solid line to CFS is treated as a thermodynamical order parameter.

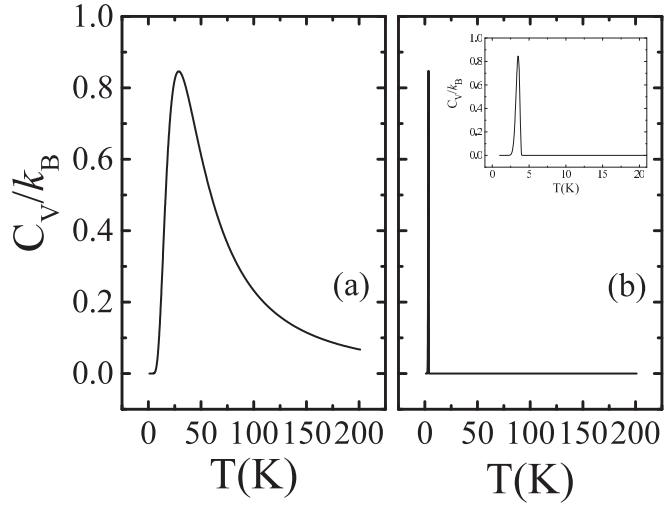

FIG. 3. Specific heat per paramagnetic Yb^{+3} ion. The low temperature part is enlarged in the inset. (a) CFS is treated as a quantum quantity. (b) CFS is treated as a thermodynamical order parameter.

potentials [32]. The cutoff energy for plane waves is set to be 600 eV. The PAW potentials contain 9 valence electrons for Yb($5p^6 5d^1 6s^2$), 13 for Mn($3p^6 3d^5 4s^2$), 11 for Y($4s^2 4p^6 4d^1 5s^2$), 3 for Al($3s^2 3p^1$), and 6 for O($2s^2 2p^4$). The 13 of the YB-4f electrons are placed in the PAW core. This is also why only 13 f electrons are considered for the paramagnetic property of Yb^{+3} ions. The exchange correlation energy was described by the generalized gradient approximation (GGA) using the PBE functional [33]. We apply an on-site Coulomb correction for the Mn-3d states following the DFT+U scheme [34] with the Dudarev implementation [35] for on-site Coulomb repulsion U and exchange interaction J. The effective Coulomb repulsion of Mn ions, $U_{\text{eff}} = 1.5$ eV from o-$LuMnO_3$ [19], reproduces the correct lattice parameters, band gap, and magnetic structure of bulk o-$YbMnO_3$. An $8 \times 4 \times 6$ and $4 \times 8 \times 6$ Γ-centered k-points sampling are used for the $\mathbf{a} \times 2\mathbf{b} \times \mathbf{c}$ and the $2(\mathbf{a} - \mathbf{b}) \times \mathbf{a} \times \mathbf{c}$ crystal cells, respectively [19]. Each self-consistent electronic calculation is converged to 10^{-6} eV and the tolerance force is set to 0.01 eV/Å for ionic relaxation. To simulate an epitaxial strain, the lattice constants $|\mathbf{a} - \mathbf{b}|$ and $|\mathbf{c}|$ of a slated crystal cell are scanned from bulk values to the values set by (110)-oriented $YAlO_3$ substrate while $\mathbf{a}$, the angle γ between $\mathbf{a}$ and $\mathbf{b}$, and atomic positions are relaxed to minimize structural energy. The ferroelectric polarization is calculated using the Berry-phase approach.

IV. RESULTS AND DISCUSSION

A. Low magnetic anomaly associated with rare-earth Yb ions

As we mentioned above, two magnetic transitions arises separately from the transition-metal Mn ions and rare-earth Yb ions, thus we discuss their origins one by one below. Using Eqs. (10) and (11) listed above, the magnetic susceptibility and specific heat of paramagnetic Yb^{+3} ions are calculated and shown in Figs. 2 and 3. As illustrated by the dashed line in Fig. 2, magnetic susceptibility with constant CFS demonstrates monotonically decreasing behaviors with temperature and no low magnetic anomaly is observed. As shown in the left panel of Fig. 3, the magnetic-related specific heat of paramagnetic Yb ions with constant CFS also shows a very broader peak associated with the thermal excitations of lower energy $J = 7/2$ multiplicity. The sharp narrow specific heat peaks typically observed in manganite based perovskites with rare-earth atoms do not show in the model with constant CFS parameters [14–17].

To investigate the thermal fluctuation effect on magnetic and thermodynamical properties, we calculated again the susceptibility and specific heat by assuming $\Delta_i(T) = \Delta_i^0(1 - T/T_C)$ with $T_C = 4$ K within the estimated range. The results are presented by the solid line in Fig. 2 and by the right panel of Fig. 3. Not surprisingly, the low magnetic anomaly appears naturally as a result of vanishing CFS order parameter above the transition temperature. We also found that a sharp narrow peak appears in the specific heat contributed by the low $J = 7/2$ multiplicity as orbital moments are freed from crystal field quenching. This specific heat peak resembles the narrow sharp peaks observed in many manganite based perovskites with rare-earth atoms. Although a quantitative comparison is difficult because the measured specific heat includes lattice, electronic, as well as magnetic contributions [14–17], we have nevertheless compared the susceptibility jump and specific heat jump between our model and experimentally measured values. For the susceptibility jump, our value is 0.201 emu/mol Oe in comparison with the experimental value of 0.135 emu/mol Oe [4]. They compare reasonably well with each other. Regarding the specific heat jump, no experimental value is available on $YbMnO_3$. However, our value 6.98 J/mol K is comparable to the value 4 J/mol K reported for $HoMnO_3$ [15].

B. Mn magnetic structures of pristine and [1$\bar{1}$0] strained o-$YbMnO_3$

As the crystal structure of o-$YbMnO_3$ is the same as that of o-$LuMnO_3$ except Yb replacing Lu, we take the same effective Hubbard $U_{\text{eff}} = 1.5$ eV on Mn-d orbitals extracted from

TABLE I. Calculated and measured crystal parameters of the E-AFM structure of o-$YbMnO_3$ and o-$YAlO_3$.

	$YbMnO_3$ This work	$YbMnO_3$ (9 K) [4] Experiment	$YAlO_3$ [19] Theory	$YAlO_3$ [36] Experiment
a (Å)	5.2255	5.2160	5.1791	5.180
b (Å)	5.8389	5.8030	5.3338	5.330
c (Å)	7.3250	7.2816	7.3815	7.375

o-$LuMnO_3$ in the following calculation [19]. The energy comparison suggests that E-AFM structure is also the magnetic ground state consistent with the experimental observation. FM, A-AFM, C-AFM, and G-AFM magnetic structures are higher in energy by 36.65, 14.08, 95.93, and 97.44 meV per double cell of 40 atoms in *Pbnm* space group. The optimized crystal parameters of E-AFM structure are summarized in Table I together with the experimental data. The discrepancy between the calculated and measured crystal parameters are all within 1%. The crystal parameters of o-$YAlO_3$ are also listed in Table I to facilitate the calculation of strained $YbMnO_3$ on $YAlO_3$ substrate.

Motivated by the magnetic transition from E-AFM structure to FM structure upon epitaxially compressive strain imposed by (110) oriented $YAlO_3$ substrate, here we show that the same scenario happens also for $YbMnO_3$ when $[1\bar{1}0]$ compressive strain is applied. In this setting, the in-plane $[1\bar{1}0]$ and [001] axes are parallel to the interface and match the lattice constants of the substrate. As shown in Table I, the lattice constant c of $YbMnO_3$ is slightly smaller than that of $YAlO_3$, the strained $YbMnO_3$ is stretched somewhat along the [001] axis and compressively strained along the $[1\bar{1}0]$ direction. We vary the crystal parameters c and $|\mathbf{a}-\mathbf{b}|$ of the strained $YbMnO_3$ linearly between those of strain-free o-$YbMnO_3$ and o-$YAlO_3$. To do so, we define the $[1\bar{1}0]$ strain as $\epsilon = (d_{1\bar{1}0} - d^0_{1\bar{1}0})/d^0_{1\bar{1}0}$ with $d^0_{1\bar{1}0} = \sqrt{a^2+b^2}$ and $d_{1\bar{1}0} = |\mathbf{a}-\mathbf{b}|$ denoting the bulk value of o-$YbMnO_3$ and the setting value of strained sample, respectively. Such a prescription of $d_{1\bar{1}0}$ is made possible by rotating the $|\mathbf{a}-\mathbf{b}|$ axis to a Cartesian x axis while expressing $\mathbf{a}$ in the xy plane. Although the atoms near the surface of the polar crystal to vacuum can have dramatic relaxation depending on the terminating atomic layer, the atomic positions of $YbMnO_3$ near the interface are essentially pinned down by $YAlO_3$ substrate. In Fig. 4(a) the energies of five typical magnetic structures are presented for a strain range $\epsilon = 0$–0.06 with $\epsilon = -0.0554$ of (110)-oriented $YAlO_3$ substrate included. Obviously the energies of C-AFM and G-AFM structures are always much higher in energy than the rest of the other structures. The ground-state magnetic structures are competing among FM, A-AFM, and E-AFM structures. The E-AFM structure is a ground state as expected in the strain-free bulk compound. As compressive strain increases, the transition takes place from the E-AFM

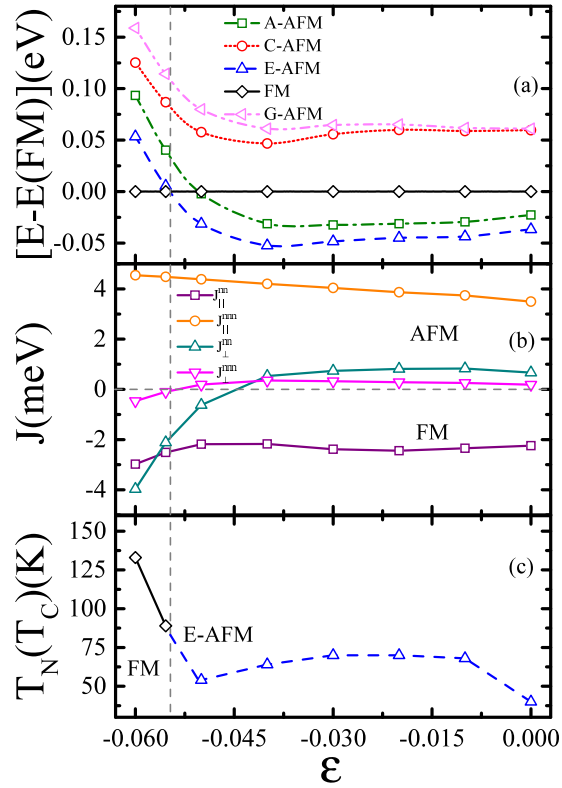

FIG. 4. The magnetic phase diagram of $YbMnO_3$ as functions of $[1\bar{1}0]$ compressive strain ϵ. Symbols are the calculated points while lines guide eyes. (a) The energies per eight formula units of five magnetic structures with the FM structure set as a reference. (b) Heisenberg exchange parameters. (c) Transition temperature. The vertical dashed line marks the strain (-0.0554) imposed by (110)-oriented $YAlO_3$ substrate.

structure of $Pmn2_1$ symmetry to a half-metal FM structure of $P21/m$ symmetry at $\epsilon = -0.0546$, a value only slightly below that imposed by $YAlO_3$ substrate. Accompanying the magnetic transition, the crystal angle γ between crystal axes $\mathbf{a}$ and $\mathbf{b}$ decreases monotonically with compressive strain ϵ. The optimized value γ for the FM structure of strained sample is tabulated in Table II. The large compressive strain corrugates the MnO_2 plane, which enhances the FM double-exchange interaction against the AFM superexchange interaction.

From the energies of five magnetic structures presented in Fig. 4(a), one is able to construct the Heisenberg Hamiltonian with normalized spin moment $H = \sum_{i,j} J_{ij}\hat{s}_i \cdot \hat{s}_j$. Following Yamauchi *et al.* [37], we considered exchange couplings for the in-plane nearest neighbor $J^{nn}_{\parallel}$, in-plane next-nearest neighbor along b axis $J^{nnn}_{\parallel}$, interplane nearest neighbor $J^{nn}_{\perp}$, and interplane next-nearest neighbor $J^{nnn}_{\perp}$. The four Heisenberg exchange coupling parameters can be derived from the energies of five magnetic structures, they are plotted in Fig. 4(b) as functions of compressive strain. As one can see,

TABLE II. The relation between the crystal angle γ and $[1\bar{1}0]$ compressive strain ϵ in the FM structure.

ϵ	0.00	−0.01	−0.02	−0.03	−0.04	−0.05	−0.0554	−0.06
γ (deg)	90.00	89.19	88.41	87.63	86.85	86.07	85.66	85.14

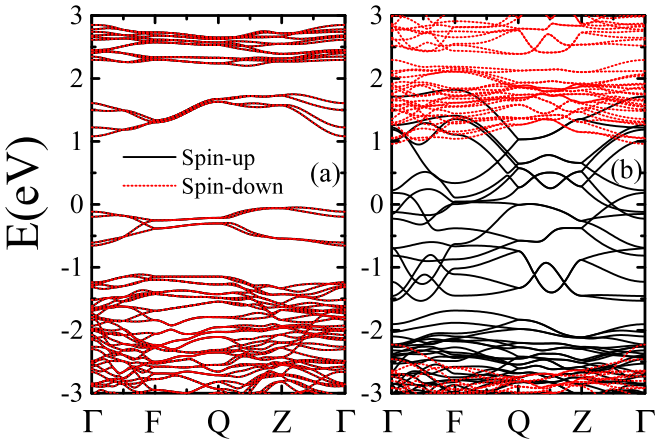

FIG. 5. The spin-resolved electronic band structures of $YbMnO_3$: (a) E-AFM structure at $\epsilon = 0$ and (b) FM structure at $\epsilon = -0.0554$. Solid lines represent the spin-up bands while dashed lines represent the spin-down bands. The band structures are computed along the high symmetrical points of the slated Brillouin zone under compressive strain with Γ(0,0,0), F(0,0.5,0), Q(0,0.5,0.5), and Z(0,0,0.5). Fermi energy is set as energy zero.

the in-plane exchange couplings are larger than the interplane exchange couplings in most of the strain range. $J_{\parallel}^{nn}$ is always ferromagnetic (negative) while $J_{\parallel}^{nnn}$ is always antiferromagnetic (positive). The interplane exchange couplings $J_{\perp}^{nn}$ and $J_{\perp}^{nnn}$ are antiferromagnetic and much weaker when compressive strain is small. However they change into ferromagnetic when $(1\bar{1}0)$ compressive strain is large. In particular, $J_{\perp}^{nn}$ can be comparable with $J_{\parallel}^{nn}$ at the strain value imposed by $YAlO_3$.

Using the Heisenberg Hamiltonian with the exchange couplings shown in Fig. 4(b), one is able to simulate thermodynamical properties of strained $YbMnO_3$ [38,39]. To do so, we carried out a Monte Carlo simulation on a lattice composed of $20 \times 20 \times 20$ Mn ions. The magnetic transition temperature is extracted from specific heat jump and drawn in Fig. 4(c). It is seen that Néel temperature representing antiferromagnetic to paramagnetic transition is relatively flat and varies between 40–70 K. The lowest $T_N = 40$ K occurs for pristine $YbMnO_3$ which is, surprisingly, very close to the observed value [4]. At high compressive strain which stabilize the ferromagnetic structure, Curie temperature (T_C) increases very rapidly as compressive strain increases further.

To view the evolution of electronic structure of $YbMnO_3$ as a function of epitaxial compressive strain, the electronic band structures of E-AFM and FM structures are shown in Fig. 5 at their stable strain values $\epsilon = 0.0$ and $\epsilon = -0.0554$, respectively. For the E-AFM structure [Fig. 5(a)], the electronic bands are degenerate with respect to electron spin and reflect antiferromagnetic nature. This state is an electronic insulator with a band gap of 1 eV. In fact, this state is also a polar state with spontaneous ferroelectric polarization $P = 1.5565\ \mu C/cm^2$ along **a** axis. Thus, it is consistent with all the features of the multiferroic compound observed in experiments. It is interesting to note that the strain stabilized FM structure is a spin fully polarized half-metal instead of an insulator, as illustrated in Fig. 5(b). An averaged magnetic moment is 4 μ_B/Mn. So one expects that there is an insulator-metal transition accompanying the E-AFM to FM transition for a uniformly compressively strained sample. Because the critical compressive strain is so close to and just below that imposed by $YAlO_3$ substrate, a coexistence of ferromagnetism near interface and antiferromagnetism away from interface can occur. The exchange-bias phenomenon would be a definite fingerprint for such a possible scenario [19].

V. CONCLUSION

In summary, we proposed in this paper that the amplitude-modulated low magnetic anomaly at 3–4 K observed in *o*-$YbMnO_3$ originated from a gradual quenching of $4f$-orbital moment of Yb ions. This is made possible by the thermal lattice vibration which smears out the intrinsically anisotropic CFS energy. Therefore, CFS energy, in principle, has to be treated as a thermodynamical order parameter. Critical temperature is defined as one where order parameter is killed by thermal fluctuation. This phenomenon is peculiar to rare-earth atoms with a partially filled f shell and small CFS energy susceptible to thermal fluctuation. Thus, the low magnetic anomaly is not only present in orthorhombic and hexagonal perovskites $RMnO_3$, but also is expected to occur in any other compounds with rare-earth elements such as dodecaborides RB_{12}. For the magnetic properties associated with Mn ions, we showed that E-AFM structure is the magnetic ground structure of $YbMnO_3$ which can also be converted into a ferromagnetic structure when $YAlO_3$ substrate is applied.

ACKNOWLEDGMENTS

This work was supported in part by the National Key R&D Program of China under Grant No. 2017YFA0303202 and the National Natural Science Foundation of China (NNSFC) under Grant No. 11474148. Part of the numerical calculations were carried out in the High Performance Computing Center (HPCC) of Nanjing University.

[1] M. Dawber, K. M. Rabe, and J. F. Scott, Rev. Mod. Phys. **77**, 1083 (2005).
[2] R. von Helmolt, J. Wecker, B. Holzapfel, L. Schultz, and K. Samwer, Phys. Rev. Lett. **71**, 2331 (1993).
[3] V. E. Wood, A. E. Austin, E. W. Collings, and K. C. Brog, J. Phys. Chem. Solids **34**, 859 (1973).
[4] Y. H. Huang, H. Fjellvåg, M. Karppinen, B. C. Hauback, H. Yamauchi, and J. B. Goodenough, Chem. Mater. **18**, 2130 (2006).
[5] H. L. Yakel, Acta Crystallogr. **8**, 394 (1955).
[6] H. L. Yakel, W. C. Koehler, E. F. Bertaut, and E. F. Forrat, Acta Crystallogr. **16**, 957 (1963).
[7] T. Kimura, S. Ishihara, H. Shintani, T. Arima, K. T. Takahashi, K. Ishizaka, and Y. Tokura, Phys. Rev. B **68**, 060403(R) (2003).
[8] M. T. Hutchings, Solid State Phys. **16**, 227 (1964).
[9] J. S. Griffith, *The Theory of Transition-Metal Ions* (Cambridge University Press, Cambridge, 1961).

[10] S. Pailhès, X. Fabrèges, L. P. Régnault, L. Pinsard-Godart, I. Mirebeau, F. Moussa, M. Hennion, and S. Petit, Phys. Rev. B **79**, 134409 (2009).
[11] H. Fukumura, N. Hasuike, H. Harima, K. Kisoda, K. Fukae, T. Yoshimura, and N. Fujimura, J. Phys.: Condens. Matter **21**, 064218 (2009).
[12] E. C. Standard, T. Stanislavchuk, A. A. Sirenko, N. Lee, and S.-W. Cheong, Phys. Rev. B **85**, 144422 (2012).
[13] X. Fabrèges, I. Mirebeau, P. Bonville, S. Petit, G. Lebras-Jasmin, A. Forget, G. Andrè, and S. Pailhès, Phys. Rev. B **78**, 214422 (2008).
[14] B. Sattibabu, A. K. Bhatnagar, S. S. Samatham, D. Singh, S. Rayaprol, D. Das, V. Siruguri, and V. Ganesan, J. Alloys Compd. **644**, 830 (2015).
[15] B. Lorenz, F. Yen, M. M. Gospodinov, and C. W. Chu, Phys. Rev. B **71**, 014438 (2005).
[16] D. O'Flynn, M. R. Lees, and G. Balakrishnan, J. Phys.: Condens. Matter **26**, 256002 (2014).
[17] F. Yen, C. dela Cruz, B. Lorenz, E. Galstyan, Y. Y. Sun, M. Gospodinov, and C. W. Chu, J. Mater. Res. **22**, 2163 (2007).
[18] H. Okamoto, N. Imamura, B. C. Hauback, M. Karppinen, H. Yamauchi, and H. Fjellvåg, Solid State Commun. **146**, 152 (2008).
[19] G. Li, X. Huang, J. Hu, G. Song, and W. Zhang, Phys. Rev. B **97**, 085140 (2018).
[20] A. Czopnik, N. Shitsevalova, A. Krivchikov, V. Pluzhnikov, Y. Paderno, and Y. Ōnuki, J. Solid State Chem. **177**, 507 (2004).
[21] J. D. Song, C. Fan, Z. Y. Zhao, F. B. Zhang, J. Y. Zhao, X. G. Liu, X. Zhao, Y. J. Liu, J. F. Wang, and X. F. Sun, Phys. Rev. B **96**, 174425 (2017).
[22] S. Chattopadhyay, V. Simonet, V. Skumryev, A. A. Mukhin, V. Yu. Ivanov, M. I. Aroyo, D. Z. Dimitrov, M. Gospodinov, and E. Ressouche, Phys. Rev. B **98**, 134413 (2018).
[23] G. A. Stewart, H. A. Salama, C. J. Voyer, D. H. Ryan, D. Scott, and H. StC. O'Neill, Hyperfine Interact. **230**, 195 (2015).
[24] G. Colizzi, A. Filippetti, and V. Fiorentini, Phys. Rev. B **76**, 064428 (2007).
[25] Z. Fang, I. V. Solovyev, and K. Terakura, Phys. Rev. Lett. **84**, 3169 (2000).
[26] C. L. Ma, Z. Q. Yang, and S. Picozzi, J. Phys.: Condens. Matter **18**, 7717 (2006).
[27] G. Colizzi, A. Filippetti, F. Cossu, and V. Fiorentini, Phys. Rev. B **78**, 235122 (2008).
[28] C. K. Jørgensen, J. Inorg. Nucl. Chem. **1**, 301 (1955).
[29] A. J. Freeman and R. E. Watson, Phys. Rev. **127**, 2058 (1962).
[30] P. Fulde and M. Lowenhaupt, Adv. Phys. **34**, 589 (1985).
[31] G. Kresse and J. Furthmüller, Phys. Rev. B **54**, 11169 (1996).
[32] P. E. Blöchl, Phys. Rev. B **50**, 17953 (1994).
[33] J. P. Perdew, K. Burke, and M. Ernzerhof, Phys. Rev. Lett. **77**, 3865 (1996).
[34] C. Loschen, J. Carrasco, K. M. Neyman, and F. Illas, Phys. Rev. B **75**, 035115 (2007).
[35] S. L. Dudarev, G. A. Botton, S. Y. Savrasov, C. J. Humphreys, and A. P. Sutton, Phys. Rev. B **57**, 1505 (1998).
[36] R. Diehl and G. Brandt, Mater. Res. Bull. **10**, 85 (1975).
[37] K. Yamauchi, F. Freimuth, S. Blügel, and S. Picozzi, Phys. Rev. B **78**, 014403 (2008).
[38] H. J. Xiang, S. H. Wei, and M. H. Whangbo, Phys. Rev. Lett. **100**, 167207 (2008).
[39] X. Ming, C. Autieri, K. Yamauchi, and S. Picozzi, Phys. Rev. B **96**, 205158 (2017).